

Static shapes of levitated viscous drops

By L. DUCHEMIN¹, J. R. LISTER¹ AND U. LANGE²

¹Department of Applied Mathematics and Theoretical Physics, University of Cambridge,
Wilberforce Road, Cambridge, CB3 0WA, UK

²Schott Glas, Mainz, Germany

(Received 24 September 2004 and in revised form 23 February 2003)

We consider the levitation of a drop of molten glass above a spherical porous mould, through which air is injected with constant velocity. The glass is assumed to be sufficiently viscous compared to air that motion in the drop is negligible. Thus static equilibrium shapes are determined by the coupling between the lubricating pressure in the supporting air cushion and the Young–Laplace equation. The upper surface of the drop is under constant atmospheric pressure; the static shape of the lower surface of the drop is computed using lubrication theory for the thin air film. Matching of the sessile curvature of the upper surface to the curvature of the mould gives rise to a series of capillary ‘brim’ waves near the edge of the drop which scale with powers of a modified capillary number. Several branches of static solutions are found, such that there are multiple solutions for some drop volumes, but no physically reasonable solutions for other drop volumes. Comparison with experiments and full Navier–Stokes calculations suggests that the stability of the process can be predicted from the solution branches for the static shapes, and related to the persistence of brim waves to the centre of the drop. This suggestion remains to be confirmed by a formal stability analysis.

1. Introduction

Some applications (e.g. manufacture of lenses) require the casting of glass drops with a very good surface quality. This can be achieved by an industrial process that avoids contact between the drop of molten glass and the mould. The mould is porous, and air is injected through it in such a manner that the glass drop lies on a thin air cushion during its solidification. Two different types of problems discourage use of this technique. The first is the existence of static ‘brim’ waves close to the outer boundary of the lens, which leads to a bad optical quality. The second is an instability, which has been observed experimentally and numerically: for some shallow mould shapes, an air bubble accumulates in the centre of the mould, which eventually breaks through the upper surface of the drop.

In order to explain the existence of brim waves near the edge of the drop and examine the source of instability, we have developed a model for the static shape of a drop levitated in a curved mould above a thin air film. Comparison with full Navier–Stokes simulations gives good agreement with both equilibrium shapes and the domain of stability. Scaling laws for the amplitude and wavelength of the brim wave are derived by adapting the analysis of Wilson & Jones (1983), and compare well with numerical results. The case of levitation above a flat plane (Goldshnik, Khanin & Ligai 1986) does not exhibit brim waves and the shape of the rim is given instead by the analysis of Jones & Wilson (1978).

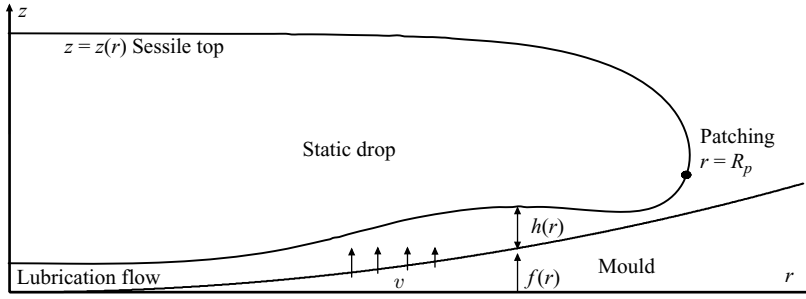


FIGURE 1. Sketch of the problem. Air is injected through the mould with Darcy velocity v . Solutions for the sessile top surface and the lubrication layer beneath are patched at $r = R_p$, and the maximum radius is $r = R$. We non-dimensionalize lengths with the capillary length $l_c = (\sigma/\rho g)^{1/2}$, so that the dimensionless top surface is given by $\kappa(r) - z(r) = \kappa(0)$.

2. Governing equations

Motivated by the large viscosity ratio, we consider the motion in the molten glass to be negligible compared to the motion in the air film, so that the pressure in the glass is hydrostatic. We can then split the problem of determining the shape of the glass drop into two parts: first, find a hydrostatic solution for the top surface, on which the external pressure is atmospheric and constant; and second, find a hydrostatic solution for the bottom surface, where the lubrication approximation is used to determine the spatial variation of the external pressure in the air film. The problem is sketched in figure 1.

2.1. The sessile top surface

On the upper surface, the external pressure is constant, so that equating the interfacial pressure jump to the hydrostatic variation in the glass gives the shape of the surface from

$$\sigma \kappa(r) - \rho g z(r) = \sigma \kappa_0, \quad (2.1)$$

where r is the distance to the axis of symmetry, z is measured from the top of the drop, ρ is the density of the glass, σ is the coefficient of surface tension and $\kappa_0 = \kappa(0)$. The curvature $\kappa(r)$ is approximated for simplicity by the two-dimensional curvature

$$\kappa(r) = \frac{z''(r)}{[1 + z'^2(r)]^{3/2}}, \quad (2.2)$$

since the large aspect ratio of a flat-lying drop allows us to neglect the azimuthal component. (Sample calculations using the full axisymmetric curvature for both top and bottom surfaces gave essentially the same results.) Equation (2.1) is subject to the boundary conditions

$$z(0) = 0, \quad z'(0) = 0, \quad (2.3)$$

and κ_0 is related to the size of the drop.

Introducing the arclength s and the angle ψ between the normal vector to the interface and the vertical, we split (2.1) into three first-order ordinary differential equations for $\psi(s)$, $r(s)$ and $z(s)$,

$$\frac{d\psi}{ds} = z(s) + \kappa_0, \quad \frac{dr}{ds} = \cos \psi, \quad \frac{dz}{ds} = \sin \psi, \quad (2.4)$$

where we have non-dimensionalized all lengths with the capillary length $l_c = (\sigma/\rho g)^{1/2}$. This system of equations is integrated using a fifth-order adaptative Runge–Kutta method, from the top of the drop to the point $r = R_p$ at which the slope $\tan \psi$ reaches the value 10. This point is slightly after the maximum radius $r = R$ of the drop, where $\psi = -\pi/2$. The shape of the upper surface and the values of R and R_p are uniquely determined by the parameter κ_0 . Once the upper surface has been computed, we patch this solution at $r = R_p$ to a lubrication model for the air film in $r < R_p$, as described below. Changing the patching point to where $\tan \psi = 5$ or 15 had a negligible effect on the results, confirming that the patching point is sufficiently far from the mould that lubrication pressure can be neglected for $r > R_p$.

2.2. The lubrication problem

Let v denote the (Darcy) injection velocity through the porous mould, and μ the dynamic viscosity of the air. The velocity v is assumed to be uniform, and not affected by the small pressure variations under the drop. By mass conservation in a steady state, the depth-integrated flux in the air film is $Q = rv/2$ (Hinch & Lemaitre 1994). Assuming the film thickness $h(r)$ to be slowly varying ($h' \ll 1$) and the mould to be almost flat, the lubrication approximation gives

$$Q = -\frac{h^3}{12\mu} \frac{\partial p}{\partial r}. \tag{2.5}$$

Since the motion in the glass is negligible, the dimensional pressure in the air is

$$p(r) = p_0 - \rho g[f(r) + h(r)] - \sigma \kappa(r), \tag{2.6}$$

where $p_0 - \rho g[f(r) + h(r)]$ is the hydrostatic pressure in the glass, with p_0 a constant; $f(r)$ is the mould shape and the curvature is again approximated by the two-dimensional curvature (2.2), with $z = f + h$ here. Combining (2.5) and (2.6) shows that the steady shape of the lower surface is given by

$$\frac{6\mu vr}{h^3} = \frac{\partial}{\partial r}(\rho g(f + h) + \sigma \kappa) \tag{2.7}$$

or, in dimensionless form,

$$6Ca = \frac{h^3}{r} \left(f + h + \frac{f'' + h''}{[1 + (f' + h')^2]^{3/2}} \right)', \tag{2.8}$$

where $Ca = \mu v/\sigma$ is the capillary number. The inclusion of terms in $(f' + h')^2$, while not necessary in the lubrication approximation, allows for a smooth matching to the sessile top surface with curvature (2.2).

The third-order equation (2.8) is also solved using an adaptive Runge–Kutta method. As boundary conditions, we require that $h'(R_p)$ and $h''(R_p)$ match to the sessile solution for the top surface, and that $h'(0) = 0$, so that the slope is zero on the axis of symmetry. In order to solve this two-point boundary-value problem, we shoot from the two conditions at $r = R_p$ (fixed by κ_0) by varying the vertical offset $h_p = h(R_p)$ until a solution is found that hits the third condition $h'(0) = 0$. For most values of κ_0 there is more than one value of h_p such that $h'(0; h_p) = 0$; the choice between alternative solutions is discussed in the following section.

Though the solutions found in this way are parameterized by κ_0 or, equivalently, by the maximum radius R , the parameter that would be controlled experimentally is the drop volume V or, equivalently, the Bond number $Bo = \rho g V^{2/3}/\sigma$. The volume is calculated from the solution for given values of κ_0 and Ca , and solutions for a given volume must be sought by inverting this relationship.

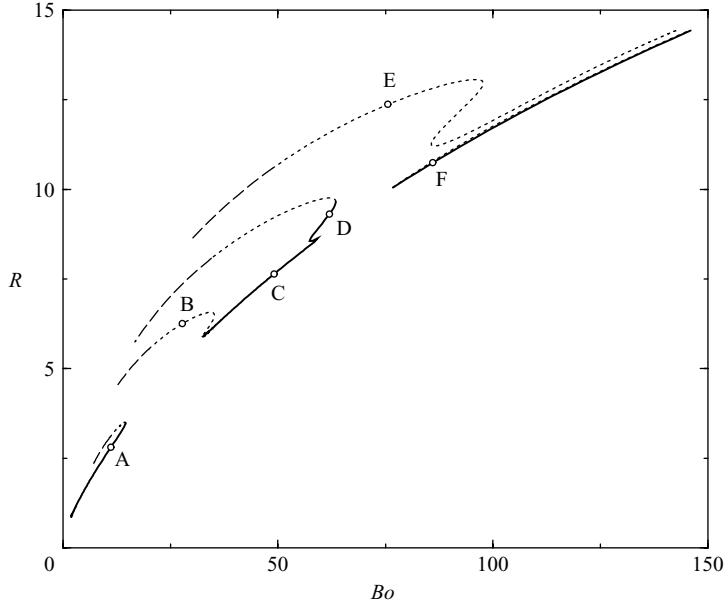


FIGURE 2. Radius of the drop R as a function of the Bond number for $Ca = 3.59 \times 10^{-5}$ in a spherical mould of radius $a_M = 50$. The shapes corresponding to the labelled points are shown in figure 3. The dashed parts of the curves correspond to unphysical shapes that self-intersect. The dotted parts correspond to shapes with large-amplitude waves on the lower surface, which are unlikely to be stable. The solid parts correspond to the smallest vertical offset h_p for a given value of Bo , give reasonable shapes and are most likely to be observed.

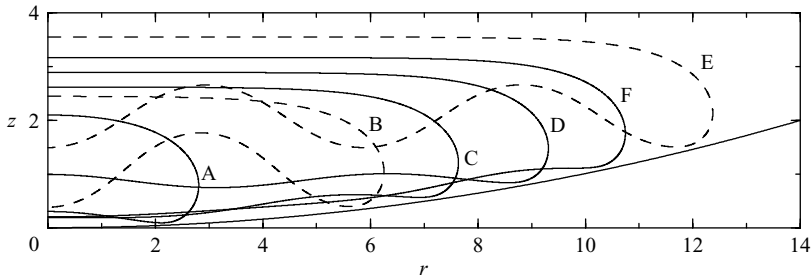


FIGURE 3. Shapes corresponding to the labelled points on figure 2. Shapes B and E (dashed) have large oscillations on the lower surface and appear unlikely to be stable.

3. Solutions

Figures 2 and 3 show typical results obtained by varying R (equivalently κ_0) at a fixed value $Ca \approx 4 \times 10^{-5}$ in a spherical mould with radius of curvature $a_M = 50$. As shown in figure 2, there can be several solutions to $h'(0; h_p) = 0$ either for a given value of R or for a given value of Bo , raising the question of which, if any, could be observed. Some parts of the solution curves (dashed) correspond to shapes for which the lower interface pierces the top surface and can thus immediately be ruled out as unphysical. Other shapes, such as those marked B and E, have such large oscillations on the lower surface that, though they do not actually intersect the upper surface, they cannot reasonably be expected to be stable. The parts of the solution curves shown as solid in figure 2 all have the smallest vertical offset h_p for these

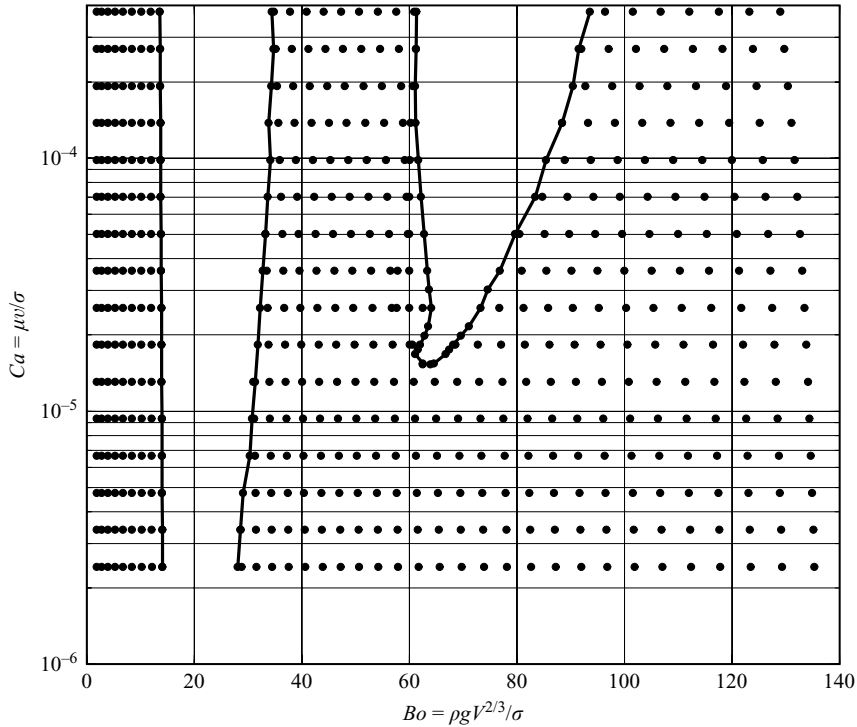


FIGURE 4. Regime diagram obtained from the lubrication solutions. The solid circles correspond to solution branches A, C, D and F (figure 2).

Bond numbers and give shapes, such as those marked A, C, D and F, which appear plausible. They also show brim waves on the lower surface of similar dimensions to those observed experimentally. If we work on the hypothesis that these solution segments are the ones likely to be observed, we note that a continuous variation of Bo could lead to discontinuous jumps to solution segments which are unphysical or implausible, which would presumably be manifested as an instability. This suggestion is explored further in §4.

Figure 4 shows the results of performing a similar analysis for a range of capillary numbers. The dots correspond to solutions from segments A, C, D and F in figure 2 and the solid lines denote the boundaries of regions where only solutions from segments B and E are available.

4. Comparison with Navier–Stokes simulations

Some simulations of the full set of Navier–Stokes equations for flow in both the glass and the air have been made with the industrial finite-element code POLYFLOW (Lange 2002). Figure 5 shows very good agreement between two of these simulations and the shapes predicted by our lubrication model. In these examples, and all the simulations of Lange (2002), the radius of curvature of the spherical mould a_M is set equal to $4.76V^{1/3}$, where V is the volume of the drop.

Some of the Navier–Stokes simulations settle to give stable shapes, but some are unstable due to growth of a trapped air bubble (figure 6). Figure 7 shows the stability diagram obtained from the POLYFLOW simulations (Lange 2002). Instability is clearly favoured by larger capillary numbers, but the alternation of stability and

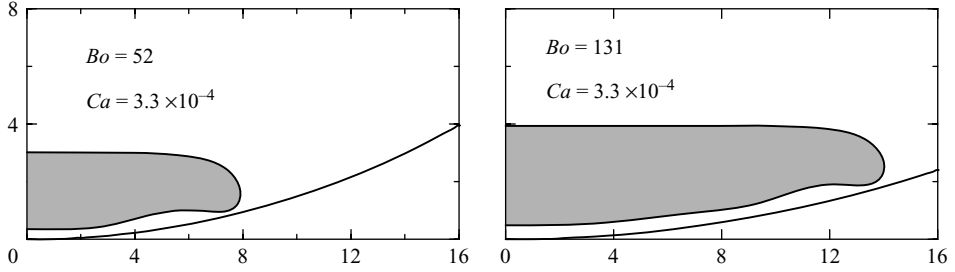


FIGURE 5. Typical comparison between stable Navier–Stokes POLYFLOW simulations (grey shapes) and our lubrication results (solid lines) for two values of $Bo = \rho g V^{2/3} / \sigma$.

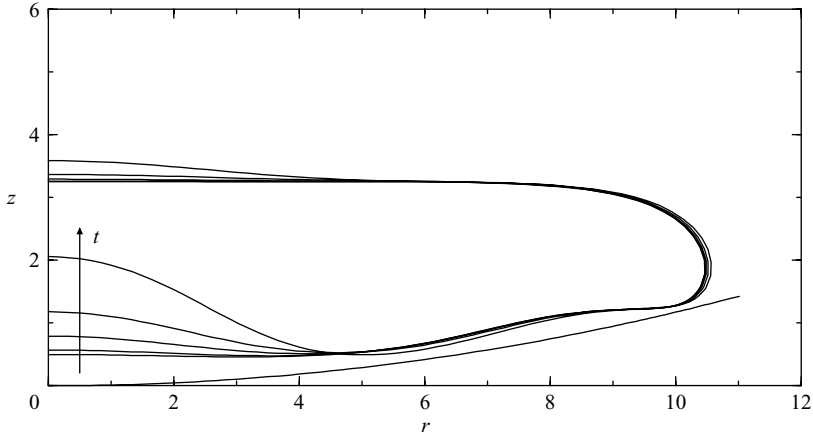


FIGURE 6. Time-dependent simulation with POLYFLOW. An unstable case, with $Ca = 6.7 \times 10^{-5}$ and $Bo = 82$.

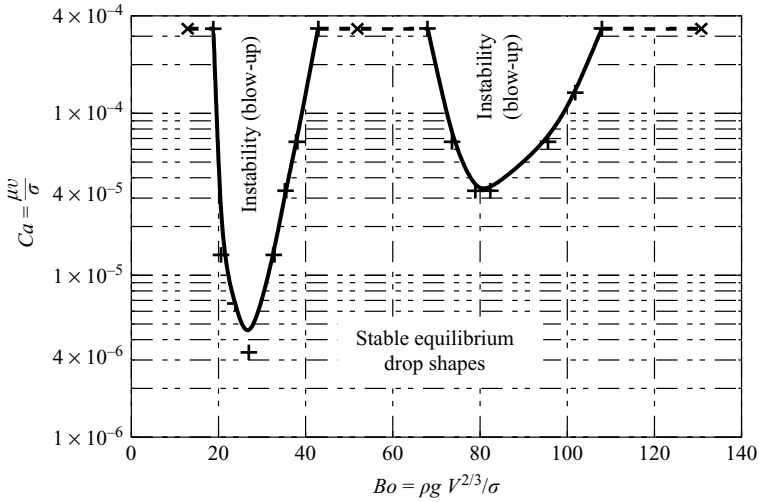


FIGURE 7. Stability diagram obtained from the POLYFLOW simulations (Lange 2002). The symbols + and \times mark stable simulations; instability is manifested by growth of a central air bubble (figure 6).

instability as the size of the drop increases was unexplained. Comparison of figures 4 and 7 suggests that stability in the time-dependent simulations is closely linked to the availability of a reasonable solution for the static shape, and supports our earlier hypothesis that segments A, C, D and F correspond to observable shapes.

Figures 4 and 7 are not exactly comparable, since the radius of curvature a_M of the mould used for the POLYFLOW computations varies with the volume of the drop, whereas our calculations require the mould shape to be specified before the drop volume can be found. Sample calculations with our model for different values of a_M suggest that variations of a_M may be sufficient to account for some of the quantitative difference between the two figures; for example, with $a_M = 25$ ($Bo = 27.6$ in Lange's simulations), we find that the gap between segments A and C is reduced from $Bo \in (15, 32)$ to $(17, 21)$ for $Ca = 4 \times 10^{-6}$, reflecting an upward shift of the first region without solutions as in figure 7. Further sample calculations for $Ca = 3.59 \times 10^{-5}$ using the full axisymmetric curvature instead of the two-dimensional approximation show that the physically reasonable solutions are essentially unaffected, and that the gap between segments A and C persists and is shifted to the right, but only by 10–15%.

The lubrication model reproduces the magnitude and wavelength of the brim waves observed in both experiments and Navier–Stokes simulations (figure 5). The ratio of the wavelength of the brim waves to R also seems to be correlated with the form of solution, with solutions from segments B and E showing one and two full oscillations respectively and solutions from segments A, C/D and F showing half, one and a half, and two and a half oscillations respectively.

5. Brim-wave scalings

The physical origin of brim waves is the need to match the sessile curvature of the top surface to the smaller curvature of the mould. The dimensions of the brim waves can be derived from an asymptotic analysis (Appendix A), in terms of the small parameter

$$\delta = (6CaF^5 R_t / l_c)^{1/3}, \quad (5.1)$$

where R_t is the radius at which the top sessile solution would contact the mould tangentially in the case of no air injection and perfect wetting, and $F = f'(R_t)$. The first nip, which is the narrow gap near the edge of the drop, has a height scaling like $\delta^{6/5} l_c / F^2$ and a width like $\delta^{3/5} l_c / F$ as $\delta \rightarrow 0$, whereas the first lobe has a height scaling like $\delta^{9/10} l_c / F^2$ and width like $\delta^{3/10} l_c / F$. These scalings were tested by varying Ca for fixed R_t and F . Figure 8 shows that the predicted scaling laws in Ca for the first nip and lobe are in very good agreement with the numerical results.

It is clear from the form of (5.1) that the results must differ for the case of a flat plane with $f \equiv 0$. As discussed in Appendix B, the succession of brim waves is replaced by a single central dimple with a nip at the edge. This nip has height scaling like $(6Ca R_t)^{2/5} l_c^{3/5}$ and width like $(6Ca R_t)^{1/5} l_c^{4/5}$. The scales are in fact the same as those of the first nip when $F \neq 0$, since the first nip is governed by $6Ca R_t \sim h^3 h'''$ with $h'' \sim 1/l_c$ in both cases. We note, however, that it is the scale of the brim-wave lobes that seems to be linked to stability.

6. Concluding remarks

Our lubrication model is in good agreement with the Navier–Stokes computations. The brim waves are reproduced and their scaling is in excellent agreement with

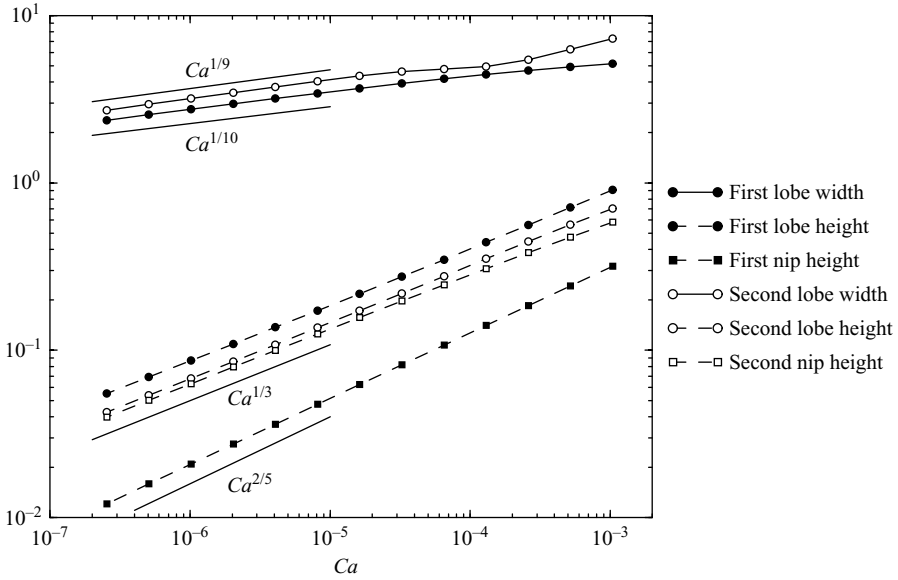


FIGURE 8. The dimensions of the first two nips and lobes from the numerical solution of (2.8), for $R_p = 13.73$ and $Bo \approx 130$. The heights of the nips and lobes are the minima and maxima of $h(r)$ respectively; the widths of the lobes are defined by the horizontal distance between two successive nips. The height of the first nip scales like $Ca^{2/5}$, as predicted; the scalings of subsequent lobes and nips are indistinguishable from the asymptotic predictions of $Ca^{1/3}$ and $Ca^{1/10}$.

an asymptotic analysis for small capillary number. The regions where there are no plausible static solutions seem to be closely correlated to the unstable regions given by the Navier–Stokes simulations. The lubrication model and the asymptotic analysis are much simpler and computationally cheaper than finite-element Navier–Stokes simulations, and can thus be used as a predictive tool. The correlation between stability and the form of the brim waves is clear, but intriguing, and should motivate future time-dependent analysis.

We are grateful to E.J. Hinch, G. Kozyreff and J.R. Ockendon for stimulating discussions of this problem, and to the MAGICAL EU grant HPRN-CT-2002-00332 for financial support (L. D.).

Appendix A. Brim waves for $Ca \ll 1$

In this appendix, we describe an asymptotic analysis for $Ca \ll 1$ of the brim waves observed in experiments, simulations and our theoretical model. We consider a shallow mould for which $f'(r) \ll 1$, and assume for $Ca \ll 1$ (small air velocity) that $h(r) \ll f(r)$ and $h'(r) \ll f'(r)$. We study the brim waves close to $r = R_t$. If $\rho g R_t^2 / \sigma \gg 1$, then the azimuthal curvature can be neglected compared to the in-plane curvature. Moreover, we can assume that $\rho g f'(r) \gg \sigma f'''(r)$. Under these assumptions, (2.7) becomes

$$6 \frac{\mu \nu r}{h^3} = \rho g f' + \sigma h''' \tag{A 1}$$

We define $x = Fr/l_c$, $X = FR_t/l_c$, $S(x) = f'(r)/f'(R_t)$ and $\phi(x) = F^2 h(r)/l_c$, where $F = f'(R_t)$ and the scalings are chosen so that the two terms on the right-hand side

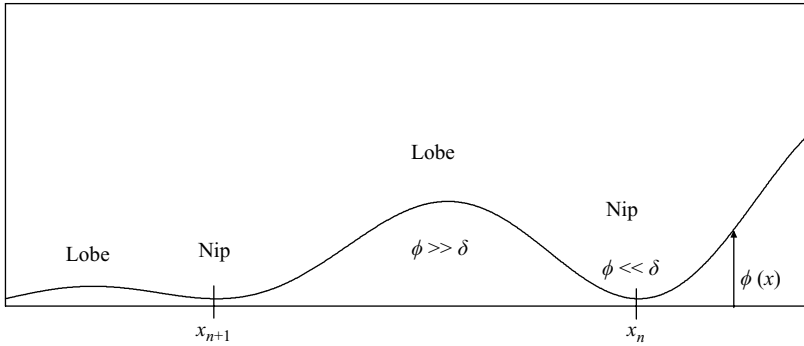


FIGURE 9. Sketch of the successive brim waves.

of (A 1) are of the same order. Expressed in these rescaled variables, (A 1) reads

$$\delta^3 \frac{x}{X} = \phi^3(S(x) + \phi'''), \tag{A 2}$$

where

$$\delta = \left(\frac{6\mu v R_t F^5}{\sigma} \right)^{1/3} \left(\frac{\rho g}{\sigma} \right)^{1/6}, \tag{A 3}$$

$S(1) = 1$ by definition, and $S(x) = x/X$ for a parabolic mould.

We are interested in asymptotic analysis of (A 2) for $\delta \ll 1$. The naive approximation $\phi = \delta$ cannot hold near the edge of the drop $x = X$ since the film thickness must be matched to the sessile curvature $\phi''(x) = 2 \cos(\theta/2) \approx 2$ for $x > X$. This matching is achieved in the region $x/X \simeq 1$ by solving

$$\delta^3 = \phi^3(1 + \phi''') \tag{A 4}$$

to find a succession of brim waves formed by lobes and nips with decreasing amplitude. We now present an asymptotic analysis of these brim waves based on a similar analysis for a falling film in Wilson & Jones (1983).

Let x_n denote the n th minimum of this solution (figure 9). Around $x = x_n$, ϕ can be assumed to be much smaller than δ , so that (A 4) reduces to

$$\delta^3 = \phi^3 \phi''' \tag{A 5}$$

(corresponding to a region of constant capillary-driven flux with $\sigma h^3 h''' / \mu = 6v R_t$).

By rescaling ϕ and x according to

$$\phi(x) = \delta^{3a_n} \Phi(\zeta), \quad x - x_n = \delta^{b_n} \zeta, \tag{A 6}$$

we obtain

$$\Phi^3 \Phi''' = 1 \quad \text{for} \quad 4a_n - b_n = 1. \tag{A 7}$$

As $\zeta \rightarrow \pm\infty$, $\Phi(\zeta) \sim \zeta$ or ζ^2 . In order that the wave amplitude decreases to the left, it is necessary that $\Phi \sim \zeta^2$ as $\zeta \rightarrow +\infty$ and $\Phi \sim \zeta$ as $\zeta \rightarrow -\infty$.

The nip is followed by a lobe in $x_{n+1} < \phi < x_n$ where $\phi \gg \delta$ and (A 4) reduces to

$$\phi''' = -1 \tag{A 8}$$

(corresponding to a capillary static balance $\rho g f' + \sigma h''' = 0$). In order to match to the adjacent nip, the solution of (A 8) must be linear at x_n and quadratic at x_{n+1} , and

hence is given by

$$\phi(x) = \frac{1}{6}(x_n - x)(x - x_{n+1})^2. \quad (\text{A } 9)$$

If $x_{n+1} - x_n \sim \delta^{\alpha_n}$, then $\phi \sim \delta^{3\alpha_n}$ in the lobe.

Matching ϕ' to the nip at x_n and ϕ'' to the nip at x_{n+1} , we obtain

$$\left. \frac{d\phi}{dx} \right|_{x_n^-} \sim \delta^{3a_n - b_n} \sim \delta^{2\alpha_n}, \quad \left. \frac{d^2\phi}{dx^2} \right|_{x_{n+1}^+} \sim \delta^{3a_{n+1} - 2b_{n+1}} \sim \delta^{\alpha_n}. \quad (\text{A } 10)$$

Combining (A 10) and (A 7b), we obtain

$$a_{n+1} = \frac{1}{10}(3 + a_n). \quad (\text{A } 11)$$

The solution for the first nip must be matched to the sessile edge of the drop, which approaches the mould with a constant curvature. Thus $a_1 = 2/5$, and we have

$$a_n = \frac{1}{3}(1 + 2 \times 10^{-n}). \quad (\text{A } 12)$$

The scalings for successive lobe heights and widths, and nip heights and widths are respectively

$$3\alpha_n = 1 - 10^{-n}, \quad \alpha_n = (1 - 10^{-n})/3, \quad 3a_n = 1 + 2 \times 10^{-n}, \quad b_n = (1 + 8 \times 10^{-n})/3,$$

and we recover the scaling laws of § 5.

Appendix B. Levitation above a plane, $f = 0$

For the case of a flat mould with $f = 0$ in the limit $Ca \ll 1$, equations (2.8) or (A 1) reduce to

$$h^3 h''' = \epsilon^5 l_c, \quad \text{where } \epsilon = (6Ca R_t / l_c)^{1/5}. \quad (\text{B } 1)$$

For $r > R_t$ we must match to the sessile curvature $h'' = 2/l_c$ of the edge of the drop. As in the problem of droplet coalescence (Jones & Wilson 1978), for $r < R_t$ we expect a thin parabolic dimple of trapped fluid, where the pressure is approximately constant, and an even thinner rim near $r = R_t$, which controls the flux leaking from the dimple to the outside. The shape of the rim is given by $h \sim \epsilon^2 l_c \varphi(\xi)$, where $\xi = (r - R_t)/\epsilon l_c$, $\varphi^3 \varphi''' = 1$, $\varphi'' \rightarrow 2$ as $\xi \rightarrow \infty$ and $\varphi'' \rightarrow 0$ as $\xi \rightarrow -\infty$; further details can be found in Jones & Wilson (1978). It should be clear that the thickness of the rim is $O(\epsilon^2 l_c)$, the width of the rim is $O(\epsilon l_c)$ and the thickness of the trapped dimple is $O(\epsilon l_c)$. The scaling of the rim is the same as that of the first nip in Appendix A for a curved mould, but the scaling of the dimple differs from that of the lobes of the brim waves.

REFERENCES

- GOLDSHTIK, M. A. & KHANIN, V. M. & LIGAI, V. G. 1986 A liquid drop on an air cushion as an analogue of Leidenfrost boiling. *J. Fluid Mech.* **166**, 1–20.
- HINCH, E. & LEMAITRE, J. 1994 The effect of viscosity on the height of disks floating above an air table. *J. Fluid Mech.* **273**, 313–322.
- JONES, A. F. & WILSON, S. D. R. 1978 The film drainage problem in droplet coalescence. *J. Fluid Mech.* **87**, 263–288.
- LANGE, U. 2002 Gas-film levitation of viscous glass droplets. ECMI Glass Days, Wattens, Austria.
- WILSON, S. D. R. & JONES, A. F. 1983 The entry of a falling film into a pool and the air-entrainment problem. *J. Fluid Mech.* **128**, 219–230.